On the constitutive modelling and damage behaviour of plain woven textile composite

Shantanu S. Mulay*, R. Udhayaraman

Department of aerospace engineering, Indian Institute of Technology Madras, Chennai 600036, India

ABSTRACT

The present work deals with the constitutive modelling and progressive failure analysis (PFA) of plain woven textile composites (PWTC). Two novel approaches, equivalent cross ply laminate (ECPL) coupled with classical laminate theory and Mori–Tanaka theory, are developed to compute homogenized properties of PWTC lamina. The PFA of PWTC lamina is performed coupling isotropic damage mechanics with ECPL theory, and *meso-scale* failure modes are identified. The novelty in the proposed PFA is that, the stress-based failure is detected, and the strain-based damage evolution is computed. A user-defined material subroutine of PFA of PWTC lamina is finally developed and test problems are solved in ABAQUS. All the simulation results of the proposed approaches are finally compared with experiments and found to be closely matching.

© 2018 Elsevier Ltd. All rights reserved.

1. Introduction

Textile composites (TC) are made by textile manufacturing processes. The unidirectional (UD) lamina usually possesses good in-plane and poor out-of-plane properties due to lack of fiber reinforcement in that direction. As compared to classical UD laminates, TC has a wider range of applications due to their good in-plane as well as out-of-plane material properties (Dixit and Mali, 2013). There are two types of yarns in woven TC: longitudinal or warp, and transverse or fill (Dixit and Mali, 2013). A pattern, consisting every warp (and fill) yarn interlaced with every alternating fill (and warp) yarn, is called plain woven textile composite (PWTC).

Material modelling of PWTC: The PWTC initially considered as a chain of 2-layered cross-ply laminates by Ishikawa (1981). The classical laminate theory (CLT) is used, ignoring fiber undulations, to compute lower and upper bounds of stiffness matrix. Ishikawa and Chou (1982) modelled longitudinal fiber undulations by a sinusoidal function ignoring fiber undulation along the transverse direction and gap between adjacent yarns. Naik and Ganesh (1995) proposed models accounting undulations along the warp and fill directions as well as the gap between adjacent yarns, but these models have complex implementation making them unsuitable to be used in a broader multiscale framework. These models also require strand width and gap parameters, which

are not uniform in a woven fabric and have to be obtained exposing laminate to scanning electron microscope (SEM). Several micromechanical-based PWTC homogenization models (Tanov and Tabiei, 2001; Wen and Aliabadi, 2009; 2010; 2011; Aliabadi, 2015) proposed in literature require complex implementation and huge computational efforts making the evaluation of stiffness matrix cumbersome. The local fiber volume fractions along the warp and fill yarns are considered equal in most of the existing models (Naik and Ganesh, 1995; 1993; Tanov and Tabiei, 2001; Wen and Aliabadi, 2009; 2010), which is physically not true for some PWTC. The present work overcomes this assumption and demonstrate the consequences of an unequal local fiber volume fraction along the warp and fill yarns. The complex existing models highlighted above require an explicit solution of boundary value problem, and may not even provide complete 3D engineering constants of PWTC (Ishikawa, 1981; Ishikawa and Chou, 1982; Naik and Ganesh, 1995). This is overcome in the present work, which analytically computes in-plane as well as entire 3D engineering constants of PWTC RVE. The regions of warp and fill yarns are considered as pure fiber bundles (Tanov and Tabiei, 2001; Wen and Aliabadi, 2009; 2010). Warp and fill yarns however really behave like UD lamina, as considered in the presented ECPL model, due to presence of matrix in-between the yarns.

Mori–Tanaka (MT) approach has also been used to compute the effective material properties of two-phase composites (Mori and Tanaka, 1973; Eshelby, 1957; Benveniste, 1987; Huysmans et al., 2004; Gommers et al., 1998; Skoček et al., 2008). Fiber undulation is usually computed by rotation tensors, which are not easy

* Corresponding author.
E-mail addresses: ssmulay@iitm.ac.in (S.S. Mulay), ae14d021@smail.iitm.ac.in (R. Udhayaraman).

to evaluate. The method proposed here computes fiber undulation angle along the warp and fill directions and transforms the Eshelby tensor accordingly. The problem of complex perturbed stress field due to yarn interlacing is circumvented in equivalent PWTC RVE (including the effect of fiber undulation), MT method is then applied treating yarns as cylindrical inclusions. The methodology adopted here is thus completely different from the existing works (Gommers et al., 1998; Skoček et al., 2008; Huysmans et al., 2004) and facilitates computation of effective engineering constants of PWTC lamina by MT method (with fiber undulation angle) to be implemented in existing multiscale codes.

Gorbatikh et al. (2007) has a detailed review on the application of damage mechanics to PWTC. The failure location in TC is found to be sensitive to the choice of failure models, but the exact modes of failure within PWTC lamina were not identified (Gorbatikh et al., 2007; Xu et al., 2015; Tabatabaei et al., 2014). The effect of in-plane shearing on PWTC lamina is largely ignored (Gorbatikh et al., 2007). This lacuna is the primary motivation for work reported in Section 5, wherein detailed failure analysis of PWTC lamina is performed under normal (along warp and fill) as well as in-plane shear loading.

The motivations are thus, (1) develop a simplified analytical methodology to compute the *homogenized* material constants of PWTC lamina in a more natural manner using CLT as well as MT methods, (2) study it's failure under various loading conditions.

The primary contributions of the present work are as follows. A novel equivalent cross-ply laminate (ECPL) model is developed first to compute *homogenized* material constants coupling it with classical laminate theory as detailed in Section 2. ECPL accounts for different fiber volume fractions along the warp and fill directions as well as constant fiber undulation angles (Udhayaraman and Mulay, 2017). Secondly, MT method is applied in a novel manner to predict entire 3D *homogenized* constants of PWTC (Section 3). A novel computation of the correct Eshelby tensor is performed including fiber undulation angle. Thirdly, The failure behaviour is studied coupling ECPL with isotropic damage mechanics (IDM) (Section 5). The *meso-scale* failure modes of PWTC lamina are thus identified under different type of loadings (tensile along warp and fill, and in-plane shear). The novelty is that, the stress-based failure is detected and strain-based damage evolution by IDM is performed at *meso-scale*, and the evolution of *macro-scale* damage is found to be anisotropic in nature. Finally, the progressive failure of PWTC lamina is obtained by user-defined material subroutine (UMAT) in ABAQUS®. The effect of the surface roughness, on maximum failure stress, is demonstrated comparing the numerical results of notched and un-notched models with *in-house* experiments as explained in Section 4. The modelling results are compared with available experimental results wherever it is possible (in-house experiments performed or available literature referred and cited).

2. Development of equivalent cross-ply laminate model for PWTC

The ECPL model of PWTC RVE is developed that is coupled with CLT to analytically compute homogenized material constants. Thus, no boundary value problems are required to be solved. All the abbreviations used in this paper are listed in Table 1 in order to facilitate a quick reference.

2.1. Formulation of ECPL model

A PWTC material is obtained embedding plain weave fiber fabric into a matrix material (polymer based or ceramics). The continuum domain of PWTC can thus be seen as a sequence of cross-ply laminates along global X and Y axes with 0° and 90° plies

alternating their positions as shown in Fig. 1(a). A spatial repeating structure or representative volume element (RVE) of PWTC can be obtained, as highlighted in Fig. 1(a), and shown in Fig. 1(c). This PWTC RVE is based on two assumptions that, the fiber undulations are ignored and the yarns are closely packed without an empty space in-between.

The RVE thus sequentially contain [0/90] and [90/0] cross-ply laminates along global X and Y axes. The averaged stiffness matrices of [0/90] and [90/0] plies, $[\overline{Q}]_1$ and $[\overline{Q}]_2$ respectively, are obtained applying CLT, and a macroscale stiffness matrix $[\overline{Q}]_{RVE}$ of RVE is obtained averaging $[\overline{Q}]_1$ and $[\overline{Q}]_2$ over a length of RVE (Ishikawa, 1981; Ishikawa and Chou, 1982; Naik and Ganesh, 1992). If all the four quadrants of PWTC RVE, as shown in Fig. 1(c), are identical in dimensions and fiber volume fractions, the matrix [B] obtained by CLT for [0/90] and [90/0] laminates will have an opposite sign. The resulting $[\overline{Q}]_{RVE}$ thus has average $[\overline{B}] = 0$ (Ishikawa, 1981; Ishikawa and Chou, 1982; Naik and Ganesh, 1992; 1995; 1993). The extensional stiffness [A] and bending stiffness [D], obtained by CLT, for [0/90] and [90/0] laminates are identical, resulting in $[\overline{Q}]_{RVE}$ with same $[\overline{A}]$ and $[\overline{D}]$ as that of [0/90] laminate (Daniel and Ishai, 2006). The lack of force-curvature and moment-strain coupling lead to conclude that, it is sufficient to convert only one-fourth portion of PWTC RVE into ECPL model while evaluating *macroscale* material constants of entire PWTC employing CLT. The ECPL model, as shown in Fig. 1(b), thus act as a bridge linking CLT with PWTC RVE involving local fiber volume fractions along the warp (0°) and fill (90°) plies, and their individual ply thicknesses as primary variables.

The warp and fill fiber plies are embedded without matrix as shown in Fig. 1(c), where the fiber and matrix phases are considered separately with the matrix phase equally divided into two plies, as shown in Fig. 1(d). It is assumed that each of the matrix plies get embedded into the warp and fill directions resulting final ECPL model as shown in Fig. 1(b).

Let length l and width w of a quarter portion of PWTC RVE is maintained in ECPL as well. The different volumes in a quarter portion of PWTC RVE are

$$V_m = (v_m)_g \underbrace{(l\,w\,t)}_{V_{RVE}}, \; V_f^W = (v_f^w)_g\,(l\,w\,t), \; V_f^F = (v_f^F)_g\,(l\,w\,t) \left.\right\}$$
(1)

where $(v_f)_g = (v_f^w)_g + (v_f^F)_g$, and $(v_m)_g$, $(v_f^w)_g$, and $(v_f^F)_g$ are the matrix, warp fiber and fill fiber volume fractions, respectively, computed with respect to the global volume of PWTC RVE, t, V_m, V_f^W, V_f^F are the values of thickness, total volume correspond to the matrix, warp fibers and fill fibers, respectively, within quarter portion of PWTC RVE, and $(v_f)_g$ is total global fiber volume fraction. The volume and mass of a single yarn, V_y and M_y respectively, are computed by *apriori* measuring total mass of fabric M_{fabric}, total number of warp and fill yarns N_W and N_F respectively, and yarn density ρ_f in a fabric mat (Udhayaraman and Mulay, 2017). The fiber volumes along the warp and fill directions within a dry fabric are then computed as

$$V_f^W = N_W\,V_y, \; V_f^F = N_F\,V_y, \text{ and } V_y = \frac{V_{fabric}}{N_W + N_F}$$
(2)

N_F and N_W are measured within fixed dimensions of plain woven fiber fabric, where it is possible to have $N_W \neq N_F$. It is assumed in Eq. (2) that all the yarns are almost identical, irrespective of their direction. The total mass of matrix M_m and matrix density ρ_m are also *apriori* measured to get the total volume of matrix $V_m = M_m/\rho_m$ (Udhayaraman and Mulay, 2017). All the global volumes given in Eq. (1) can be computed and the total volume of a quarter portion of PWTC RVE is thus computed as $V_{RVE} = (l\,w\,t) = V_m + V_f^W + V_f^F$. All the global volume fractions are also computed

Table 1
List of abbreviations.

Abbreviation	Meaning	Abbreviation	Meaning
TC	Textile composites	UD	Unidirectional
PWTC	Plain woven textile composite	CLT	Classical laminate theory
3D	Three dimensional	MT	Mori–Tanaka
RVE	Representative volume element	SEM	Scanning electron microscope
ECPL	Equivalent cross-ply laminate	IDM	Isotropic damage mechanics
GP	Gauss point	VM	Voigt–Mandel
ECPL + CLT	ECPL model coupled with CLT	UMAT	User-defined material subroutine
PWTC + MT	PWTC RVE coupled with MT	PFA	Progressive failure analysis
WiU	Without undulation	SU	Sinusoidal undulation
CU	Constant undulation	NU	No undulation
WU	With undulation	CCW	Counterclockwise
MSF	Maximum stress failure	KP	Knee points
2D	Two dimensional	DIC	Digital image correlation
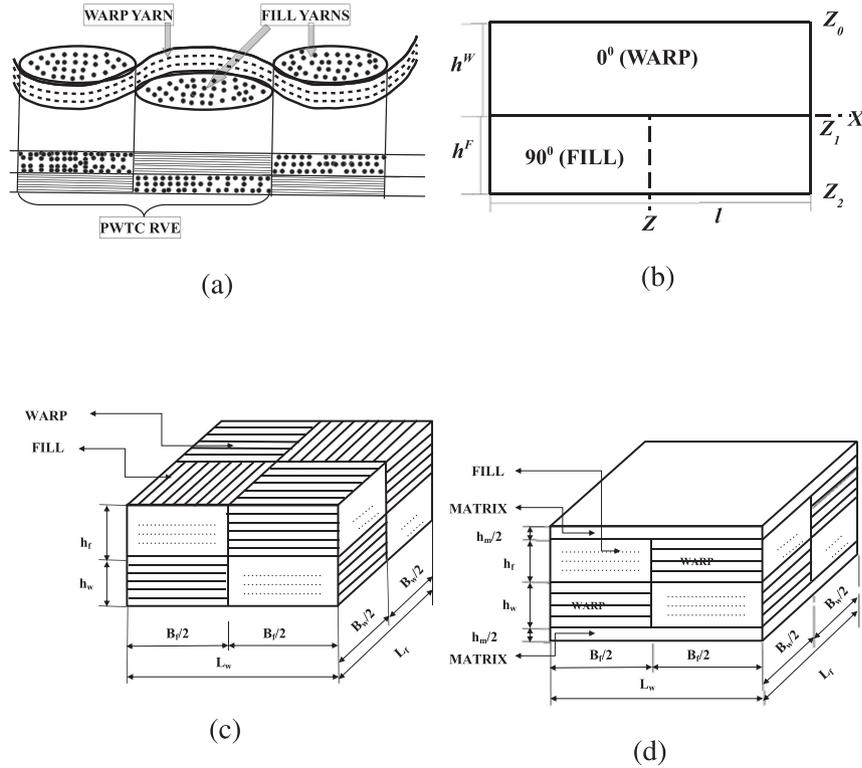
Fig. 1. (a) PWTC as a chain of alternating cross-ply laminates, (b) ECPL model, (c) Complete PWTC RVE (without matrix), (d) modified PWTC RVE.

by Eq. (1), dividing each individual global volume by V_{RVE}. The total volume of warp and fill plies is computed as

$$\left.\begin{array}{l} (V^{wp})_l = V_f^W + \dfrac{V_m}{2} \Rightarrow (V^{wp})_l = V_{RVE}\left[(v_f^w)_g + \dfrac{(v_m)_g}{2}\right] \\[2mm] (V^{Fp})_l = V_f^F + \dfrac{V_m}{2} \Rightarrow (V^{Fp})_l = V_{RVE}\left[(v_f^F)_g + \dfrac{(v_m)_g}{2}\right] \end{array}\right\} \quad (3)$$

where $(V^{wp})_l$ and $(V^{Fp})_l$ are the total *local* volumes along the warp and fill plies, respectively. Let $(v_f^w)_l$ and $(v_f^F)_l$ be the *local* fiber volume fractions along the warp and fill plies, respectively, with respect to the respective local total volumes $(V^{wp})_l$ and $(V^{Fp})_l$, as

given

$$\left.\begin{array}{l} (v_f^w)_l = \dfrac{V_f^W}{(V^{wp})_l} \Rightarrow (v_f^w)_l = \dfrac{(v_f^w)_g}{\left[(v_f^w)_g + \dfrac{(v_m)_g}{2}\right]}, \\[4mm] (v_f^F)_l = \dfrac{V_f^F}{(V^{Fp})_l} \Rightarrow (v_f^F)_l = \dfrac{(v_f^F)_g}{\left[(v_f^F)_g + \dfrac{(v_m)_g}{2}\right]} \end{array}\right\} \quad (4)$$

where Eqs. (1) and (3) are substituted in Eq. (4). Let $\mathcal{V}^{wp}$ and $\mathcal{V}^{FP}$ be the warp and fill ply volume fractions with respect to ECPL as

Table 2
Nomenclature of variables used in ECPL model.

Variable	Meaning
l, w, t	length, width and thickness of quarter portion of PWTC RVE
V_m, V_f^W, V_f^F	volumes of matrix, warp fibers, and fill fibers
	in quarter portion of PWTC RVE
$(v_m)_g, (v_f^w)_g, (v_f^F)_g$	global volume fractions of matrix, warp fibers and fill fibers
$(v_f)_g$	global fiber volume fraction
V_{RVE}	total volume of RVE
V_y, M_y	volume and mass of single yarn
$M_{fabric}, V_{fabric}, \rho_f$	mass of fabric, volume of fabric, yarn density
N_W, N_F	total number of warp and fill yarns in a fiber mat
M_m, ρ_m	matrix mass and density
$(V^{wp})_l, (V^{Fp})_l$	local volumes of warp and fill plies
$(v_f^w)_l, (v_f^F)_l$	local fiber volume fractions within warp and fill plies
$\mathcal{V}^{wp}, \mathcal{V}^{Fp}$	warp and fill ply volume fractions
h^w, h^F	warp and fill ply thicknesses
h^{cp}	ECPL thickness
$(X, Y, Z), (1, 2, 3)$	global and local (principal material) axis system

$$\mathcal{V}^{wp} = \frac{(V^{wp})_l}{V_{RVE}} \Rightarrow \left[(v_f^w)_g + \frac{(v_m)_g}{2}\right], \mathcal{V}^{Fp} = \frac{(V^{Fp})_l}{V_{RVE}} \Rightarrow \left[(v_f^F)_g + \frac{(v_m)_g}{2}\right] \Bigg\} \quad (5)$$

where Eq. (3) is substituted in Eq. (5). The warp and fill ply thicknesses h^w and h^F, respectively, within ECPL are computed as

$$\left. \begin{array}{l} (V^{wp})_l = l\,w\,h^w \Rightarrow (v_f^w)_l = \frac{V_f^W}{(V^{wp})_l} = \frac{(v_f^w)_g\,(l\,w\,t)}{l\,w\,h^w} \Rightarrow h^w = \frac{(v_f^w)_g}{(v_f^w)_l}\,t \\[3mm] (V^{Fp})_l = l\,w\,h^F \Rightarrow (v_f^F)_l = \frac{V_f^F}{(V^{Fp})_l} = \frac{(v_f^F)_g\,(l\,w\,t)}{l\,w\,h^F} \Rightarrow h^F = \frac{(v_f^F)_g}{(v_f^F)_l}\,t \end{array} \right\} \quad (6)$$

The Z axis ply co-ordinates in Fig. 1(b) are computed by Eq. (6). The complete ECPL model is thus developed which can be analyzed employing CLT. All the variables used in the development of ECPL model are listed in Table 2 for a quick reference. The implementation details and the results of ECPL model are discussed in the next section.

2.2. Implementation and results of ECPL model

Two co-ordinate systems are defined while analysing the RVE of PWTC. The global co-ordinate system (X, Y, Z) or (x, y, z) is defined similar to CLT (Daniel and Ishai, 2006). The local or principal material-axis system $(1 - 2 - 3)$ of PWTC lamina is defined as 1-along the warp, 2-along the fill, and 3-out-of-plane direction of lamina. Both systems coincide in the absence of off-axis lamina.

Different length scales, referred in the subsequent section, are defined as follows. A single PWTC lamina is considered at *macro-scale*, and the warp and fill plies are considered at *meso-scale*, whereas PWTC laminate is considered at *macro-scale* and a single PWTC lamina in it is considered at *meso-scale*.

The proposed ECPL model is tested by *in-house* experiments (as explained in Section 4). All ECPL model variables are computed and given in Table 5 with Z−coordinates $Z_0 = -0.33$, $Z_1 = 0.0132$, $Z_2 = 0.33$ (in mm) as shown in Fig. 1(b).

The *meso-scale* compliance matrices of plies in Voigt-Mandel (VM) form (Appendix A) are developed by mechanics-of-materials-based approach by newly proposed parallel-series model (non-linear) to compute the transverse material properties of a ply (Udhayaraman and Mulay, 2017) (E_2 and G_{12}). The *macro-scale* constants of PWTC lamina, as given in Table 6, are computed by ECPL coupling with CLT. All the variables used for the PWTC material are listed in Table 3 for a quick reference. It is seen in Table 6 that the values obtained by *ECPL model coupled with CLT* (ECPL + CLT) are slightly higher than the corresponding experimental values, and $\overline{E}_X \neq \overline{E}_Y$ because $(v_f^w)_g \neq (v_f^F)_g$. This is attributed, by post-processing of data, to two primary factors. The presence of micro-cavities and rough edges (machining), as seen in Fig. 4, and the

exclusion of fiber undulations in ECPL model. The fiber undulations lead to lower stiffness of material along the fiber direction (Udhayaraman and Mulay, 2017). The ECPL model defines constitutive response at a *macro-scale* integration or Gauss point (GP) in PWTC material assuming defect-free deterministic RVE (homogenized deformation) (Gitman et al., 2007). The presence of geometric nonlinearities (eg. edge notch), except the fiber undulations, is thus can not be explicitly included in the ECPL model. The effect of fiber undulations is included in *PWTC RVE coupled with MT method* (PWTC + MT) (Section 3), and ABAQUS® user defined material (UMAT) program is written to simulate *macro-scale* PWTC material with a small notch (dominant edge defect) (Section 5).

The variation of in-plane constants of PWTC lamina with respect to $(v_f^w)_g$ is studied deriving close-form expressions using CLT (Daniel and Ishai, 2006) as

$$\left. \begin{array}{l} \overline{E}_X = \left(\frac{h^w}{h^{cp}}\right)\left(\frac{\left[(E_1 + E_2)^2 - 4\,(\nu_{12}\,E_2)^2\right]}{\left[(E_1 + E_2)\,(1 - \nu_{12}\,\nu_{21})\right]}\right), \overline{E}_X = \overline{E}_Y, (v_f^F)_g = (v_f^w)_g \\[3mm] \overline{\nu}_{XY} = \frac{2\,\nu_{21}\,E_1}{(E_1 + E_2)}, \ \overline{G}_{XY} = G_{12}, \ \text{and} \ h^w = h^F = \frac{h^{cp}}{2} \end{array} \right\} \quad (7)$$

where h^w and h^{cp} $(h^{cp} = h^w + h^F)$ are the warp ply and ECPL thickness values, respectively, and E_1, E_2, G_{12}, ν_{12} and ν_{21} are warp ply *meso-scale* constants in it's principal material co-ordinates. The constants given in Eq. (7) are plotted in Fig. 2(a) varying $(v_f^w)_g$ and noted that $\overline{\nu}_{XY}$ initially decreases, then increases due to nonlinear variation in E_2. The off-axis PWTC lamina constants are computed by Tables 5 and 6 using Eq. (8) (Appendix A) and plotted in Fig. 2(b).

$$\mathcal{S} = R^{-1}\,S_{eng} \Rightarrow S_{VM} = \mathcal{M}\,\mathcal{S}\,\mathcal{M}^{-1} \Rightarrow \overline{S}_{VM} = (Q_s)_{VM}^T\,S_{VM}\,(Q_s)_{VM} \ \Big\} \quad (8)$$

All values in Fig. 2(b) do not converge to 1 at $\theta = 90°$ as $\overline{E}_X \neq \overline{E}_Y$ in Table 6. The ECPL model is compared with Tanov and Tabiei (2001), and Wen and Aliabadi (2009, 2010), and all the results are given in Tables 7 and 8, respectively. It is observed in Tables 7 and 8 that *macro-scale* $\overline{G}_{XY}$ value is underestimated, and the primary reason could be the consideration of smallest RVE constituent in different models of PWTC material. It is observed by open literature that, different homogenization models expect different input variables to be provided by the user. It is thus difficult to use exact input variables of one model and substitute them into other model for the purpose of comparison. The Graphite/epoxy composite input variables provided in Tanov and Tabiei (2001) and Wen and Aliabadi (2009, 2010) correspond to graphite yarn (may contain some matrix) properties. The present authors, for the purpose of comparison, considered them to be the graphite fiber properties

Table 3
Nomenclature of variables used for PWTC material.

Variable	Meaning
E, G, ν	Young's modulus, Shear modulus, Poisson's ratio
$E_1, E_2, G_{12}, \nu_{12}, \nu_{21}$	in-plane material constants of a ply in local axes
$E_{1f}, E_{2f}, G_{12f}, \nu_{12f}, E_m, \nu_m$	material constants of fiber f and matrix m
$\overline{E}_X, \overline{E}_Y, \overline{E}_Z, \overline{G}_{XY}, \overline{G}_{XZ},$	*macro-scale* constants of PWTC lamina
$\overline{G}_{YZ}, \overline{\nu}_{XY}, \overline{\nu}_{XZ}, \overline{\nu}_{YZ}$	in global axes
$(\bullet)^*, \overline{(\bullet)}$	quantity in GPa, quantity defined in global axes
σ, ϵ	stress and strain components
$\epsilon'_{VM}, \sigma'_{VM}$	VM form strain and stress components in local axes
$\epsilon_{VM}, \sigma_{VM}$	VM form strain and stress components in global axes
ϵ'_T, σ'_T	tensorial strain and stress components in local axes
$\epsilon'_{eng}, \sigma'_{eng}$	engineering strain and stress components in local axes
$\mathcal{S}$	4th-order compliance tensor relating ϵ'_T and σ'_T
S_{eng}	compliance matrix relating ϵ'_{eng} and σ'_{eng}
$S_{VM}, \overline{S}_{VM}$	2nd-order compliance tensor in local and global axes (in VM form)
$\mathcal{M}$	matrix relating tensorial components of stresses (also strains) to corresponding VM components
R	matrix relating tensorial components of strain to engineering components
$(Q_s)_{VM}$	2nd-oder transformation matrix in VM form relating global to local axes
S^w_{VM}, S^F_{VM}	Eshelby tensors for warp and fill fibers in VM form

(a)

(b)

(c)

(d)
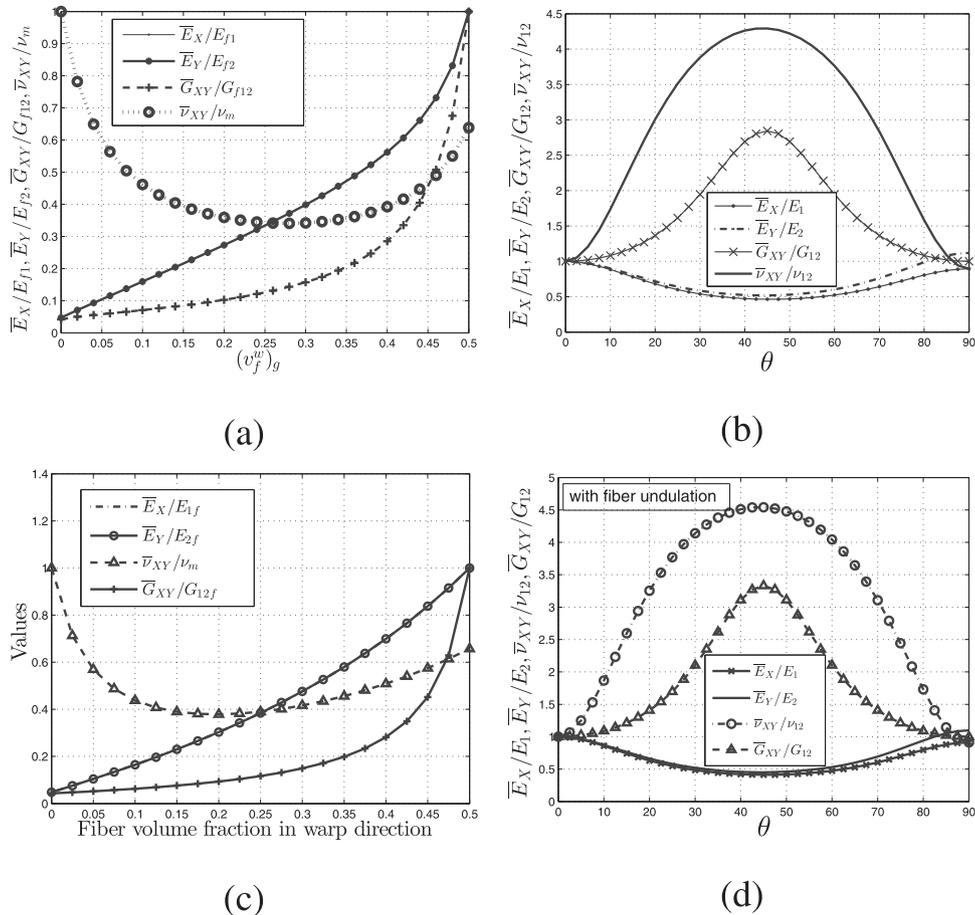
Fig. 2. (a) *Macro-scale* constants of PWTC lamina varying $(v^w_f)_g$ and CCW rotation angle θ (a, b) ECPL + CLT, (c, d) PWTC + MT WU.

(smallest micro-scale constituent is fiber in present work, and not yarn that may contain some matrix material). It can be seen in Table 8 that, the *macro-scale* properties computed by the proposed model closely match with the already reported values. The global fiber volume fraction, along the warp and fill plies of PWTC RVE, also considered equal in Table 8.

The inclusion of fiber undulation requires transformation about Y axis (Udhayaraman and Mulay, 2017), thus can not by fully cap-

tured in ECPL model (possible for $\bar{E}_X$ and $\bar{E}_Y$ but not for $\bar{G}_{XY}$). This limitation of ECPL model is overcame by coupling PWTC RVE with MT method in the next section.

3. Homogenized material constants of PWTC by Mori–Tanaka approach

Entire 3D effective material constants of PWTC lamina are computed in this section coupling PWTC RVE with MT method (Hill, 1965; 1963; Mori and Tanaka, 1973; Li et al., 2010). MT is one of the mean-field theory approaches with a detailed discussion given in Bohm (2016), Benveniste (1987) and Eshelby (1957).

3.1. Formulation of MT approach for PWTC RVE

The PWTC lamina is treated as a matrix containing warp and fill fibers as cylindrical (ellipsoidal) inclusions with separate Eshelby tensors (Eshelby, 1957).

$$S^w_{VM} = \begin{bmatrix} 0 & 0 & 0 & 0 & 0 & 0 \\ t_3 & t_1 & t_2 & 0 & 0 & 0 \\ t_3 & t_2 & t_1 & 0 & 0 & 0 \\ 0 & 0 & 0 & 2t_5 & 0 & 0 \\ 0 & 0 & 0 & 0 & 2t_4 & 0 \\ 0 & 0 & 0 & 0 & 0 & 2t_4 \end{bmatrix}, S^F_{VM} = \begin{bmatrix} t_1 & t_3 & t_2 & 0 & 0 & 0 \\ 0 & 0 & 0 & 0 & 0 & 0 \\ t_2 & t_3 & t_1 & 0 & 0 & 0 \\ 0 & 0 & 0 & 2t_4 & 0 & 0 \\ 0 & 0 & 0 & 0 & 2t_5 & 0 \\ 0 & 0 & 0 & 0 & 0 & 2t_4 \end{bmatrix} \Bigg\} \quad (9)$$

The inclusions and matrix are assumed to be homogeneous and transversely isotropic, and homogeneous and isotropic, respectively. The compliance matrices of warp and fill fibers are developed as Daniel and Ishai (2006) and Udhayaraman and Mulay (2017). The concentration and Eshelby tensors for warp and fill fibers are developed. The warp and fill fibers are along global $1-$ and $2-$axes, respectively. The planes $2-3$ and $1-3$ thus become planes of isotropy for warp and fill fibers, respectively. The respective Eshelby tensors in VM form are given in Eq. (9) (Benveniste, 1987; Mori and Tanaka, 1973), where

$$t_1 = \frac{(5-4\nu)}{8(1-\nu)}, \, t_2 = \frac{(4\nu-1)}{8(1-\nu)}, \, t_3 = \frac{\nu}{2(1-\nu)}, \, t_4 = (1/4), \, t_5 = \frac{(3-4\nu)}{8(1-\nu)} \Bigg\} \quad (10)$$

where ν is Poisson's ratio of matrix material. An effective stiffness matrix is finally computed (Bohm, 2016; Daniel and Ishai, 2006), with the implementation details and results as discussed in the next section.

3.2. Implementation and results of PWTC lamina coupled with MT approach

The MT approach is implemented by Table 5, and *macro-scale* constants of PWTC are given in Table 6 under column *without undulation* (WiU).

The *macro-scale* material constants of PWTC RVE are computed varying $(\nu^w_f)_g$ $((\nu^w_f)_g = (\nu^F_f)_g)$ and plotted in Fig. 3(a) and (b). The *macro-scale* constants of an off-axis PWTC lamina are computed $((\nu^w_f)_g = (\nu^F_f)_g = 0.25)$, and plotted in Fig. 3(c) and (d). The balanced behaviour of PWTC lamina is predicted as $\bar{E}_X = \bar{E}_Y (\bar{\nu}_{XY} = \bar{\nu}_{YX})$, $\bar{\nu}_{XZ} = \bar{\nu}_{YZ}$, and $\bar{G}_{XZ} = \bar{G}_{YZ}$ is always true.

It is concluded that PWTC lamina possess six linearly independent *macro-scale* material constants in principal material co-ordinates provided that $(\nu^w_f)_g = (\nu^F_f)_g$, and warp and fill fibers perpendicular to each other (balanced orthotropic material). It is thus concluded that the approaches ECPL + CLT and PWTC + MT predict similar *macro-scale* behaviours of PWTC lamina closely matching with experiments (Daniel and Ishai, 2006).

3.3. Results of PWTC RVE coupled with MT method including fiber undulations

Udhayaraman and Mulay (2017) recently proposed several novel approaches to include the fiber undulation effects on PWTC lamina. Different undulation approaches: sinusoidal undulation (SU), constant undulation (CU), and no undulation (NU) (Udhayaraman and Mulay, 2017) are combined firstly with ECPL model coupled with Voigt approximation (Voigt, 1889) and secondly PWTC + MT. All nine *macro-scale* constants of PWTC lamina are extracted and found to be almost equal.

The CU angle approach is adopted, and the fiber undulation angles for the *in-house* experimental studies are found to be 6.7° and 7.8° (Udhayaraman and Mulay, 2017) for the warp and fill fibers, respectively. The warp and fill fiber matrices are firstly developed in principal material co-ordinates. The warp fiber undulation effect is included by counterclockwise (CCW) rotating stiffness matrix about positive Y axis (6.7°) as in Eq. (20). The fill fiber stiffness matrix is CCW rotated about positive Y axis (7.8°) followed by 90° CCW rotation about positive Z axis as given in Eq. (18). Similar transformations are performed on the respective Eshelby tensors S^F_{VM} and S^w_{VM}. The transformation of Eshelby tensors by fiber undulation angle is one of the important contributions of the present work.

The *macro-scale* material constants of PWTC lamina, for an experimental data given in Table 5, are given in Table 6 under column *with undulation* (WU). It is noted in Table 6 that, Young's moduli with fiber undulation are slightly lower than ignoring fiber undulation, which is expected as the fiber stiffness along loading direction get off-set due to undulations. It is also seen in Table 6 that the fiber undulation only influences the principal direction stiffness values, leaving other stiffness matrix terms largely unaffected.

The *macro-scale* in-plane constants of PWTC lamina are computed by PWTC + MT WU, using parameters given in Table 5, and plotted in Fig. 2(c) and (d), and found to be same by ECPL + CLT shown in Fig. 2. It is thus shown that $(\nu^w_f)_g = (\nu^F_f)_g$ lead to three (3) independent in-plane material constants. The *macro-scale* material constants adjust such that the ratio $m = (\bar{\nu}_{XZ}/\bar{E}_X) = (\bar{\nu}_{YZ}/\bar{E}_Y)$ remain constant irrespective of rotation θ about Z axis, such that strain ϵ_{ZZ} always remain constant for equal loading along X or Y axes. It is also observed from Fig. 2(d) that, $\bar{E}_X = 2\bar{G}_{XY}(1 + \bar{\nu}_{XY})$ is satisfied by homogenized constants of PWTC for $\theta = 22.5° (2n-1)$, where $n = 1, 2, 3, \ldots$. This implies, PWTC off-axis lamina shows isotropy in $X-Y$ plane for a specific CCW rotation θ. The PWTC + MT is applied to different materials with the results given in Tables 7 and 8.

The *in-house* experimental details (specimen preparation, testing, and SEM analysis) of PWTC laminate are provided in the next section.

4. Experimental tests on PWTC material

The *in-house* experimental results of PWTC material are briefly discussed in this section (Udhayaraman and Mulay, 2017). There are several quantities, as given in Table 9, that have to be measured while preparing PWTC specimen. The measured quantities
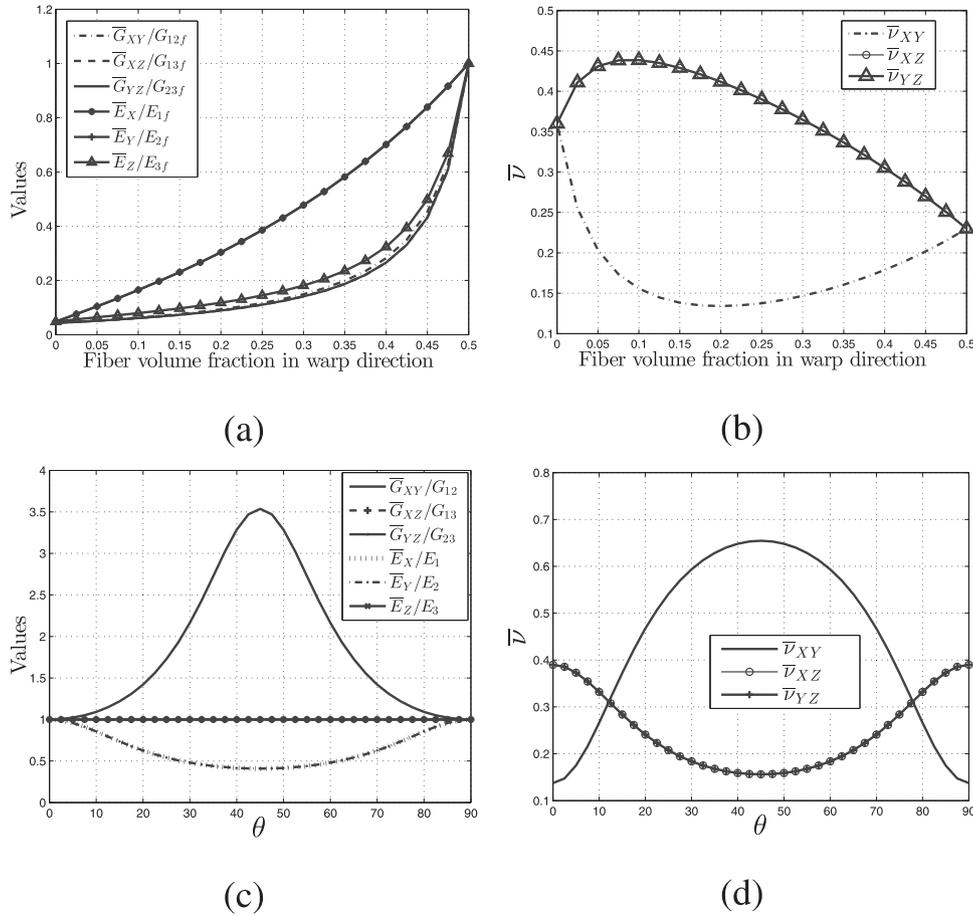
Fig. 3. *Macro-scale* properties varying $(\nu_f^w)_g$ (a) and (b), and varying in-plane angle θ (c) and (d), PWTC + MT ignoring fiber undulation.

of all the input variables are used in the proposed ECPL model and all the required variables, as given in Table 5, are computed. All the densities are measured by water displacement method Society, and fiber and matrix materials are identified as E-glass and LY556 Araldite (epoxy), respectively, with their *micro-scale* properties as in GmbH (2007) and Daniel and Ishai (2006). A PWTC specimen of thickness 2.64 mm is prepared with 4 plies resulting in $t = 0.66$ mm. Several rectangular specimens along the longitudinal (warp) and transverse (fill) directions of PWTC laminate are cut according to the dimensions given in Table 10. Four tabs are fixed along the ends of the specimen with the same adhesive, such that the specimen can be firmly held within machine jigs. The dimensions of the tabs have to be appropriately chosen such that the required load must be correctly transferred to the specimen without causing any slip (or crushing) between tabs and machine jigs.

All the specimens are then tested under uniaxial tension by 100 KN hydraulic Instron machine (INSTRON 8801) with 0.5 mm/min. displacement rate. The strain field within specimen is measured by digital image correlation (DIC) technique with a single camera. The camera is focussed normal to the thickness of the specimen, such that X and Z direction strains are measured. The measured values of material constants and ultimate σ and ϵ are mentioned in the appropriate tables.

A small portion of laminate from the fractured PWTC specimen is extracted by abrasive diamond cutter, and analyzed under SEM at low vacuum conditions. Some of the representative SEM images for both the specimens (warp and fill loading) are shown in Fig. 4, and they are analysed in the next section based on the results of progressive failure analysis of PWTC lamina.

The progressive damage analysis of PWTC lamina is performed in the next section by ECPL + CLT, in which the *meso-scale* failure modes are captured by isotropic damage mechanics (Lemaitre, 1985).

5. Progressive failure analysis of PWTC by isotropic damage mechanics

A progressive failure analysis (PFA) of PWTC lamina is performed in this section combining IDM with ECPL + CLT. Damage D is a *meso-scale* state variable that captures the initiation and evolution of defects in materials at *micro-scale* (Lemaitre, 1985; Chow and Wang, 1987; Shahabi and Forouzan, 2017).

A novel contribution of the present work is an identification of *meso-scale* failure modes (at any given GP), along the warp and fill directions, responsible for *macro-scale* failure (*macro-crack* initiation at any given GP) in PWTC material. All the variables used in the PFA of PWTC are listed in Table 4 for a quick reference.

5.1. Proposed methodology of the PFA of PWTC lamina

The PWTC material is considered at *macro-scale* level, the *meso-scale* PWTC RVE is considered to be present at any *macro-scale* GP. The warp and fill ply stresses, in principal material co-ordinates, are computed by *macro-scale* strain assuming isostrain condition. The individual ply strengths are *apriori* computed, by local fiber volume fractions, using micromechanics-based strength theories (Daniel and Ishai, 2006). Five in-plane strengths are considered for
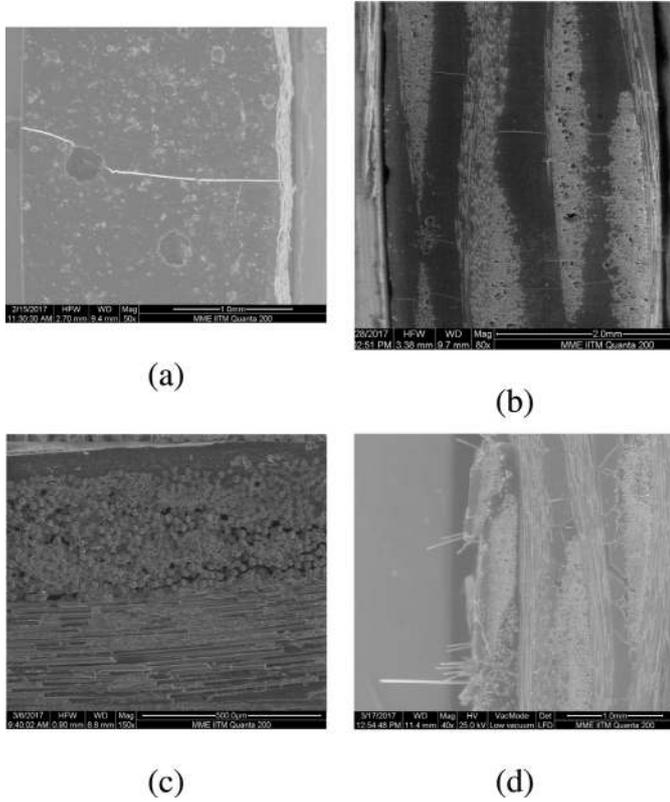
Fig. 4. SEM images (a) matrix crack towards Y axis in the top surface $(X - Y)$ while loading along warp (X axis), (b) matrix crack along Z axis $(X - Z)$ through the fill yarns while loading along warp, (c) fiber-matrix debonding in $X - Z$ plane while loading along fill (Y axis), (d) crack along X axis while loading along fill.

Table 4
Nomenclature of variables used in PFA of PWTC material.

Variable	Meaning
C^0, C^D	original undamaged, and damaged stiffness matrices
ϵ_0, κ	failure strain, and maximum strain reached so far
D	*meso-scale* damage variable
ϵ_f	parameter controlling softening region of stress - strain plot
D_{11}^{wp}, D_{22}^{wp}	warp ply damage parameters in local longitudinal, and transverse axes
ϵ_{1u}^{wp}, ϵ_{2u}^{wp}	warp ply failure strains in local longitudinal, and transverse axes
ϵ_{xx}, ϵ_{yy}	strain components in global X, and Y axes
D_{11}^{FP}, D_{22}^{FP}	fill ply damage parameters in local longitudinal, and transverse axes
ϵ_{1u}^{FP}, ϵ_{2u}^{FP}	fill ply failure strains in local longitudinal, and transverse axes
$\{\epsilon\}$, $\Delta\epsilon$	an incremental strain vector, and incremental strain value
$[\mathbf{D}]$, $\mathbf{I}$	2nd-order *macro-scale* damage tensor, and Identity matrix
Q_{RVE}, $(S_{RVE})^0$	damaged stiffness matrix, and undamaged compliance matrix of PWTC RVE
$\Delta\gamma_{XY}$	an incremental shear strain value
γ_{wf}, γ_{Ff}	shear softening parameters for warp, and fill plies
γ_{12u}^{wp}, γ_{12u}^{FP}	shear failure strains in warp, and fill plies
γ_{xy}	global shear strain component

Table 5
Parameters computed while *preparing* PWTC specimen for ECPL model.

Parameter	Value	Parameter	Value	Parameter	Value
$(v_f)_g$	0.4	ν^{wp}	0.52	ν^{Fp}	0.48
$(v_f^w)_l$	0.4231	$(v_f^F)_l$	0.375	$(v_f^w)_g$	0.22
$(v_f^F)_g$	0.18	$(v_m)_g$	0.6	h^w	0.3432 (mm)
h^F	0.3168 (mm)	–	–	–	–

each ply, namely tensile and compressive strength both along the local longitudinal (F_{1t}, F_{1c}) as well as transverse (F_{2t}, F_{2c}) directions, and $1 - 2$ plane shear strength (F_6). Maximum stress failure (MSF) theory is applied in principal co-ordinates to predict failure in plies.

The model equations for ply strength (or actual experimental values) given in Daniel and Ishai (2006) are used, and MSF theory is briefly discussed (Daniel and Ishai, 2006). The application of IDM theory to PWTC lamina is then discussed in-details.

5.1.1. Maximum stress failure theory

The MSF theory enables the understanding of failure modes in PWTC RVE, which may not be true for other failure models for anisotropic materials, eg. Tsai–Wu theory, in which an effective stress is computed (Daniel and Ishai, 2006).

The MSF theory for 2D state of stress, in the principal material co-ordinates $(1 - 2 - 3)$ of UD lamina, is expressed as Daniel and Ishai (2006)

$$F_{1t} \leq \sigma_1 \leq F_{1c}, \ F_{2t} \leq \sigma_2 \leq F_{2c}, \ |F_6| = \sigma_{12} \tag{11}$$

where σ_1, σ_2 and σ_{12} are transformed stresses, at any specific strain increment, from global $(X - Y - Z)$ to principal material co-ordinates.

5.1.2. Application of IDM to PWTC lamina

The damaged stress state in warp and fill plies is obtained by IDM as Lemaitre (1985) $\sigma_i = (1 - D) C_{ij}^0 \epsilon_j$ where σ and ϵ are *meso-scale* VM values, C_{ij}^0 and $C^D = (1 - D) C^\circ$ are original undamaged and damaged VM stiffness matrices, respectively, and $D (0 \leq D \leq 1)$ is a scalar damage parameter. An exponential evolution of D is computed separately for the warp and fill plies (as well separately along the local longitudinal and transverse directions) (Jirasek and Marfia, 2005)

$$D = \begin{cases} 0, & \kappa < \epsilon_0 \\ 1 - \dfrac{\epsilon_0}{\kappa} \, exp\left[-\dfrac{(\kappa - \epsilon_0)}{(\epsilon_f - \epsilon_0)} \right], & \epsilon_0 \leq \kappa \leq \epsilon_f \end{cases} \tag{12}$$

where ϵ_0 is a failure strain (correspond to failure stress), ϵ_f is a softening parameter (controlling slope), and κ is a maximum strain reached. The novelty is that, stress-based failure is detected, strain-based damage evolution is performed.

The parameter D is computed separately in warp and fill plies based on failure modes. The parameters D_{11}^{wp} and D_{22}^{wp} for warp ply local longitudinal and transverse failure, respectively, are defined as

$$D_{11}^{wp} = 1 - \left[\frac{\epsilon_{1u}^{wp}}{\epsilon_{xx}} \right] exp\left[\frac{-(\epsilon_{xx} - \epsilon_{1u}^{wp})}{(\epsilon_f - \epsilon_{1u}^{wp})} \right], \ D_{22}^{wp} = 1 - \left[\frac{\epsilon_{2u}^{wp}}{\epsilon_{yy}} \right] exp\left[\frac{-(\epsilon_{yy} - \epsilon_{2u}^{wp})}{(\epsilon_f - \epsilon_{2u}^{wp})} \right] \tag{13}$$

where ϵ_{1u}^{wp} and ϵ_{2u}^{wp} are failure strains in local warp longitudinal (global X) and transverse (global Y) directions, respectively, ϵ_{xx} and ϵ_{yy} are global strain components along global X and Y axes, respectively. The parameters D_{11}^{FP} and D_{22}^{FP} for fill ply local longitudinal and transverse failure, respectively, are defined as

$$D_{11}^{FP} = 1 - \left[\frac{\epsilon_{1u}^{FP}}{\epsilon_{yy}} \right] exp\left[\frac{-(\epsilon_{yy} - \epsilon_{1u}^{FP})}{(\epsilon_f - \epsilon_{1u}^{FP})} \right], \ D_{22}^{FP} = 1 - \left[\frac{\epsilon_{2u}^{FP}}{\epsilon_{xx}} \right] exp\left[\frac{-(\epsilon_{xx} - \epsilon_{2u}^{FP})}{(\epsilon_f - \epsilon_{2u}^{FP})} \right] \tag{14}$$

where ϵ_{1u}^{FP} and ϵ_{2u}^{FP} are failure strains in local fill longitudinal (global Y) and transverse (global X) directions, respectively. Eq. (12) is thus applied to warp and fill plies in a novel manner, the C^D are computed and *macro-scale* stiffness of PWTC RVE is computed by CLT.

The results of PFA of PWTC lamina (at GP), employing IDM and MSF theories, are discussed in the next section.

Table 6
Experimental Comparison of *macro-scale* constants of PWTC (* in GPa).

Approach	$\overline{E}_X^*$	$\overline{E}_Y^*$	$\overline{E}_Z^*$	$\overline{G}_{XY}^*$	$\overline{G}_{XZ}^*$	$\overline{G}_{YZ}^*$	$\overline{v}_{XY}$	$\overline{v}_{XZ}$	$\overline{v}_{YZ}$
Experiment	18.3	15.6	–	–	–	–	–	–	–
ECPL + CLT	21.02	18.8	–	3.1	–	–	0.133	–	–
PWTC + MT (WU)	21.5	19.2	8.4	2.72	2.69	2.69	0.14	0.42	0.44
PWTC + MT (WiU)	23.3	21	8.7	2.73	2.62	2.6	0.14	0.41	0.42

Table 7
Comparison of *macro-scale* constants of PWTC lamina with Tanov and Tabiei (2001) $\left((v_f)_g = 0.35\right.$ and $\theta = 9.5°$, E-glass/Epoxy) (* in GPa).

Parameter	Four-cell (Tanov and Tabiei, 2001)	Single-cell (Tanov and Tabiei, 2001)	ECPL + CLT	PWTC + MT
$\overline{E}_{XX}^*, \overline{E}_{YY}^*$	17.8	18.2	17.91	17.1
$\overline{G}_{XZ}^*, \overline{G}_{YZ}^*$	2.5	2.3	–	2.55
$\overline{v}_{XZ}, \overline{v}_{YZ}$	0.33	0.39	–	0.44
$\overline{E}_{ZZ}^*$	9.8	7.8	–	7.5
$\overline{G}_{XY}^*$	3.53	3.41	2.88	2.53
$\overline{v}_{XY}$	0.172	0.174	0.133	0.13

Table 8
Comparison of *macro-scale* constants of PWTC with Tanov and Tabiei (2001) and Wen and Aliabadi (2009, 2010) $\left((v_f)_g = 0.58\right.$ and $\theta = 1.4°$, Graphite/Epoxy) (* in GPa).

Models	$\overline{E}_{XX}^*, \overline{E}_{YY}^*$	$\overline{E}_{ZZ}^*$	$\overline{G}_{XY}^*$	$\overline{G}_{YZ}^*, \overline{G}_{XZ}^*$	$\overline{v}_{YZ}, \overline{v}_{XZ}$	$\overline{v}_{XY}$
ECPL + CLT	44.75	–	2.79	–	–	0.052
PWTC + MT	49.33	10.2	2.71	2.5	0.47	0.06
Four-cell (Tanov and Tabiei, 2001)	45.08	10.12	3.815	2.763	0.46	0.056
Single-cell (Tanov and Tabiei, 2001)	45.17	9.782	3.813	2.585	0.478	0.054
Smooth fiber I (Wen and Aliabadi, 2009)	46.48	9.343	3.58	2.78	0.49	0.052
Smooth fiber II (Wen and Aliabadi, 2009)	46.29	9.176	3.5	2.834	0.496	0.052
Model I (MLPG) (Wen and Aliabadi, 2010)	44.86	9.338	3.546	2.53	0.49	0.054
Model II (MLPG) (Wen and Aliabadi, 2010)	44.84	9.228	3.46	2.509	0.49	0.054

Table 9
Experimental measurements for PWTC specimen.

Quantity	Variable	Quantity	Variable
Weight of fabric (kg)	m_f	weight of matrix (kg)	m_m
Weight of laminate (kg)	m_c	dimensions (mm)	L, W, T
Yarn density (gm/cm³)	ρ_f	matrix density (gm/cm³)	ρ_m
Laminate effective density (gm/cm³)	ρ_c		

Table 10
Warp and fill specimen dimensions.

Specimen	Dimensions (L, W, T) (in mm)	Specimen	Dimensions (L, W, T) (in mm)
Warp	179, 18.64, 2.64	fill	245, 14.61, 2.66

Table 11
PFA of PWTC lamina by loading along X axis (* in MPa).

Parameter KP (% ϵ_{XX}, σ_{XX}^*)	Experiment (in-house)	ECPL + CLT (Gauss point)	ECPL + CLT (UMAT)
RVE 1st KP	(0.5, 100)	(0.55, 115.6)	(0.55, 117.4)
Warp 1st KP	–	(0.55, 183.1)	(0.55, 185.9)
Fill 1st KP	–	(0.55, 42.5)	(0.55, 43.2)
RVE 2nd KP	(1.47, 265.6)	(2.35, 402.8)	(1.43, 270)
Warp 2nd KP	–	(2.35, 774.7)	(1.43, 475)

5.2. Results of the PFA of PWTC lamina

The PFA of PWTC lamina (at GP) is performed applying incremental strain vector, damage computed if MSF criterion satisfied.

5.2.1. Longitudinal loading (global X axis) of PWTC lamina

An incremental strain vector $\{\epsilon\} = \{\Delta \epsilon \ (-\overline{v}_{XY} \Delta \epsilon) \ 0\}$ where $\Delta \epsilon = 1 \times 10^{-4}$, is applied on PWTC RVE with variables and *micro-scale* properties given in Table 5 and Daniel and Ishai (2006), respectively. The warp and fill softening parameters are (0.0245 and 0.0055) and (0.0245 and 0.006), respectively, for longitudinal and transverse failures with the results shown in Fig. 5(a).

Two *meso-scale* modes of failure, or knee points (KP) are detected: fill ply transverse (global X axis) failure at $\epsilon_x = 0.55\%$, and warp ply longitudinal (global X axis) failure at $\epsilon_x = 2.35\%$. It is seen in Fig. 5(a) that, once fill ply fails at $\epsilon_x = 0.55\%$, *macro-scale* stress within PWTC RVE decreases till $\epsilon_x = 0.94\%$ (till $\sigma_x \approx 0$ in fill ply), it again starts increasing due to warp ply support. It is seen in Fig. 5(d) and (b) that, *meso-scale* damage results in *macro-scale* bi-axial stress state ($\sigma_{yy} \neq 0$) and anisotropic damage in PWTC RVE. One can take recourse of the concept of effective stress, associated with the principle of strain equivalence for linear elasticity, while analysing *macro-scale* damage given as Lemaitre (1985)

$$[\mathbf{D}] = \mathbf{I} - Q_{RVE} \, (S_{RVE})^0 \tag{15}$$

where $[\mathbf{D}]$ is 2nd-order damage tensor, $\mathbf{I}$ is an identity matrix, and Q_{RVE} and $(S_{RVE})^0$ are damaged stiffness and undamaged compliance matrices of PWTC RVE, respectively. The evolution of the diagonal components of $\mathbf{D}$ is plotted in Fig. 5(b) to see that *macro-scale* damage begins in a plane normal to Y axis ($D(2, 2)$) due to failure in fill ply, and ends in a plane normal to X axis ($D(1, 1)$) due to failure in warp ply.

The simulation results of the PFA of PWTC lamina are compared with experiments given in Table 11 to find that, 1st KP is correctly predicted while the ultimate values are highly over-predicted. The presence of defects lead to lower experimental values, which are
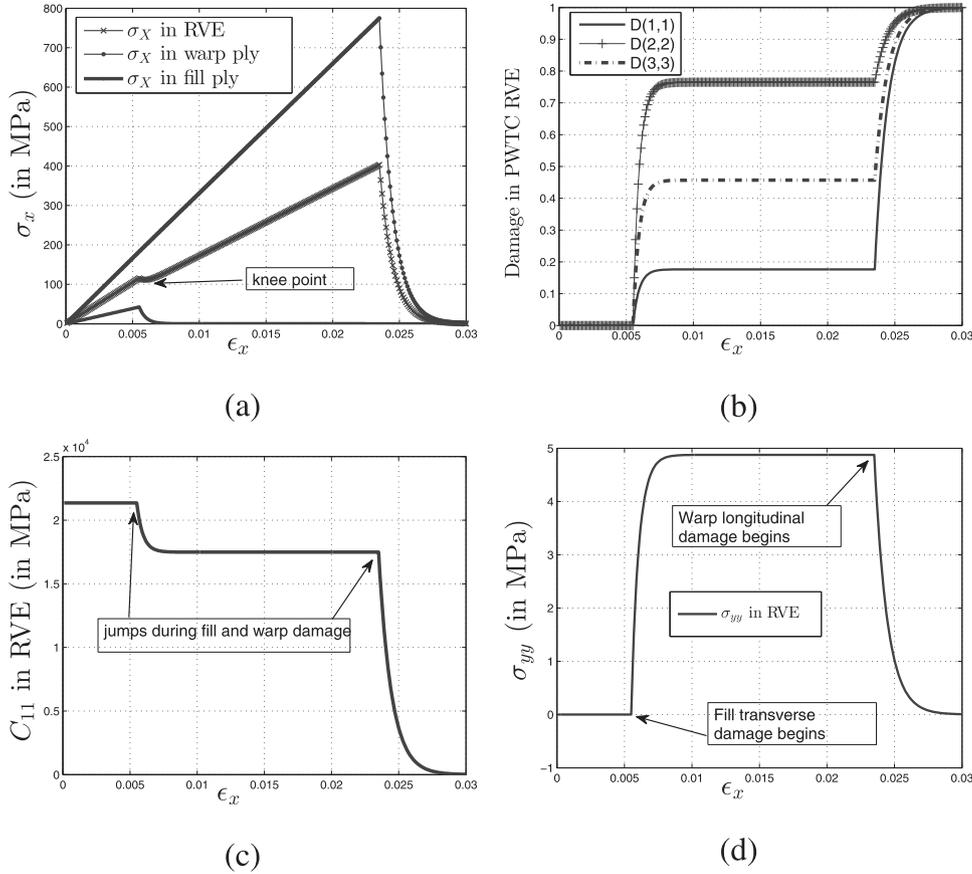
Fig. 5. PFA of PWTC RVE loading along X axis, (a) σ_{xx} vs ϵ_{xx} plots, (b) *macro-scale* damage, variation of (c) C_{XX} component and (d) σ_{yy}.

not included in PWTC + CLT. A small notch (representative of dominant crack) PWTC model will be simulated later by ABAQUS® UMAT.

5.2.2. Transverse loading (global Y axis) of PWTC lamina

An incremental strain vector $\{\epsilon\} = \{(-\overline{\nu}_{YX} \, \Delta \, \epsilon) \, \Delta \, \epsilon \, 0\}$ where $\Delta \, \epsilon = 1 \times 10^{-4}$, is applied on PWTC RVE with variables and *micro-scale* properties given in Table 5 and Daniel and Ishai (2006), respectively. All softening parameters, given earlier in Section 5.2.1, are used with the results shown in Fig. 6.

Two *meso-scale* KP are detected: warp ply transverse (global Y axis) failure at $\epsilon_{yy} = 0.48\%$, and fill ply longitudinal (global Y axis) failure at $\epsilon_{yy} = 2.35\%$. This failure behaviour is similar to the one earlier observed in Section 5.2.1. Bi-axial stress state exist in PWTC RVE once damage begins (Fig. 6(c)), and *macro-scale* damage is anisotropic (Fig. 6(d)).

5.2.3. Shear loading (plane X − Y) of PWTC lamina

An incremental strain vector $\{\epsilon\} = \{0 \; 0 \; (\Delta\gamma_{XY})\}$ where $\Delta \, \gamma_{XY} = 1 \times 10^{-5}$ is applied on PWTC RVE with variables and *micro-scale* properties given in Table 5 and Daniel and Ishai (2006), respectively. The warp and fill softening parameters are $\gamma_{wf} = 0.00625$ and $\gamma_{Ff} = 0.0075$, respectively, with the damage evolution given as

$$\left.\begin{aligned} (D_{12})^{wP} &= 1 - \left[\frac{\gamma_{12u}^{wP}}{\gamma_{xy}}\right] exp\left[-\frac{(\gamma_{xy} - \gamma_{12u}^{wP})}{(\gamma_{wf} - \gamma_{12u}^{wP})}\right], \\ (D_{12})^{FP} &= 1 - \left[\frac{\gamma_{12u}^{FP}}{\gamma_{xy}}\right] exp\left[-\frac{(\gamma_{xy} - \gamma_{12u}^{FP})}{(\gamma_{Ff} - \gamma_{12u}^{wP})}\right] \end{aligned}\right\} \quad (16)$$

where γ_{12u}^{wP} and γ_{12u}^{FP} are shear failure strains in warp and fill plies, respectively, and γ_{xy} is a global shear strain component.

All results are shown in Fig. 7 and KP are given in Table 13. Two *meso-scale* failure modes are present: warp and fill plies in-plane $(1 - 2)$ shear failures at $\gamma_{xy} = 0.62\%$ and 0.72%, respectively. The shear failure is controlled by matrix phase (Daniel and Ishai, 2006), which is present more in fill than warp ply (Table 5) (fill ply stronger in shear loading than warp). The ultimate shear stress in RVE corresponds to 1st KP as shown in Fig. 7(a), which is different from other loading cases.

All results of the PFA of PWTC lamina are summarized as follows. When PWTC lamina is loaded in global X axis, a fill ply plane having only matrix and normal to global X axis, fails first resulting in pure matrix cracking as seen in Fig. 4(b). A warp ply plane having fiber and matrix, normal to global X axis, fails resulting in PWTC lamina failure. When PWTC lamina is loaded along global Y axis, a warp ply plane having only matrix and normal to global Y axis, fails first. A fill ply plane having both fiber and matrix, normal to global Y axis, fails resulting in PWTC lamina failure (fiber-matrix debonding failure in SEM Fig. 4(c)). When PWTC lamina is loaded in global X − Y plane, a warp ply plane having fiber and matrix, parallel to global X − Y plane, fails first. A fill ply plane having fiber and matrix materials, parallel to global X − Y plane, fails resulting in PWTC lamina failure.

It is seen in Tables 11–13 that, 1st KP is correctly captured, the *macro-scale* ultimate values are over-predicted. A notched bar PWTC material model (dominant *macro-scale* crack) is thus solved in next section by ABAQUS® UMAT.

5.2.4. PFA of PWTC material by UMAT subroutine

The ECPL + CLT model coupled with IDM is implemented as UMAT subroutine. 2D notched bar (meshed) of PWTC material with length and height 10 and 1 units, respectively, is shown in
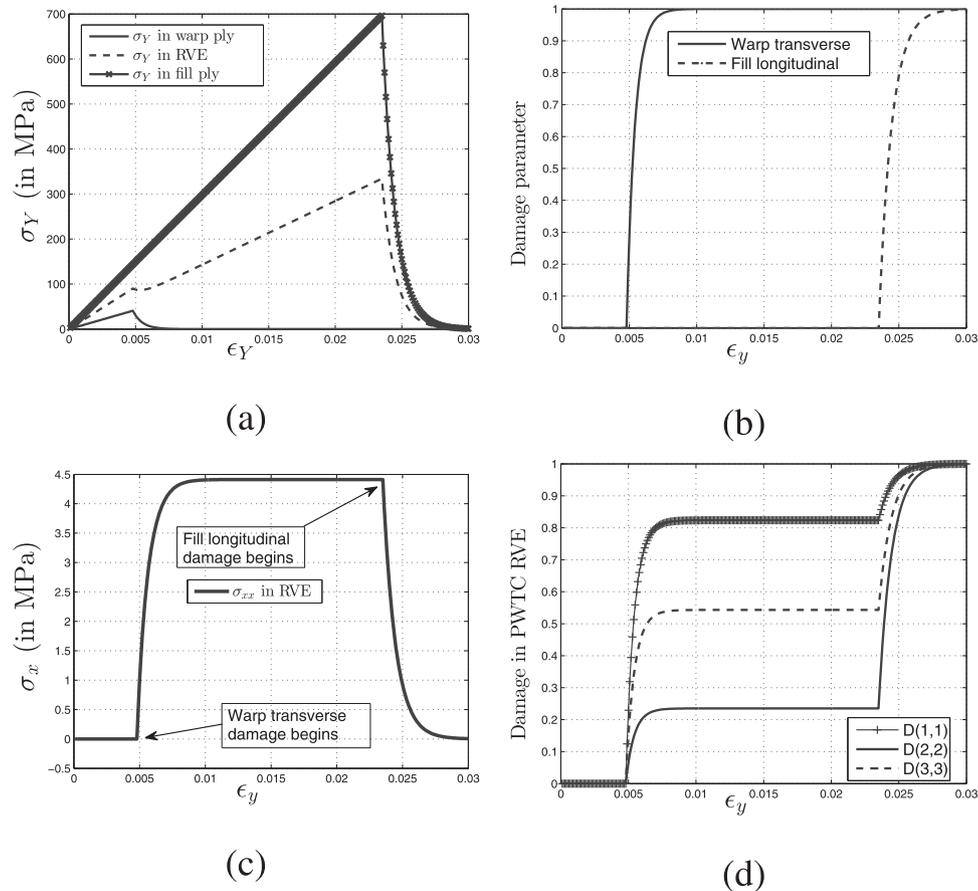
Fig. 6. PFA of PWTC loading along *Y* axis, (a) all σ_{yy} vs ϵ_{yy} plots, and evolution of (b) *meso-scale* damage, (c) σ_{xx} and (d) *macro-scale* damage components.

Fig. 8(a), and PWTC RVE is (*meso-scale*) present at every *macro-scale* GP. A small edge notch is considered (8% area reduction) representing a *macro-scale* dominant crack generated due to machining of a specimen. The horizontal and vertical displacements are constrained along the left and bottom edges, respectively, of a bar.

The *homogenized* stiffness matrix at a specific GP of PWTC material (obtained by coupling ECPL model with CLT and IDM) is a tangent matrix till no damage is detected within the corresponding *meso-scale* PWTC RVE. The *homogenized* stiffness matrix becomes secant matrix upon damage initiation at a specific GP. The required consistent tangent matrix in UMAT is thus approximated by secant matrix in the damaged state at any *macro-scale* GP. This approximation works till the ultimate *macro-scale* σ is reached, i.e., till any one of GP within a model completely fails. The *macro-scale* softening behaviour (after ultimate stress) of PWTC material model is consequently not captured by this UMAT. The results obtained by this approximation within proposed UMAT are still acceptable and serves the purpose, as all the KP values and ultimate σ and ϵ values are correctly captured (values used in engineering design of PWTC material).

The 2D notched bar model is discretized by 2084 2D plane-stress triangular elements (ABAQUS® type CPS3, 3 nodes / element, and 1 GP / element) and loaded along the right edge by a displacement along the global *X* axis. The deformation and von Mises stress distribution in bar is shown in Fig. 8, and KP values are obtained from an element (centroid) located along the loading boundary and given in 4th column of Table 11. The experimental values are *macro-scale* values, and are fairly represented by loading edge element. The KP values correspond to notch tip element are found to be same as given in 3rd column of Table 11 irrespec-

tive of the mesh size as shown in Fig. 9(b). This is an expected behaviour, because whenever any element is fully failed, it has to have KP values as given in column 3 of Table 11 (same constitutive behaviour of fully failed element independent of mesh). However, the far-field element KP values are mesh dependent. The appropriate mesh should be the one that results in far-field element KP values close to the experiments in the presence of a fixed size notch. The degree of mesh refinement (*h*-refinement), for a given size of a notch, can be identified that gives far-field (loading boundary) element KP values representing actual experimental fields. This statement is confirmed by the authors performing several numerical experiments. The KP values in crack tip and edge elements are observed for a fixed notch size (8%) and varying degree of mesh refinement as shown in Fig. 9. It is seen that all the KP values in boundary (loading edge) element lie on a same *macro-scale* $\sigma - \epsilon$ plot (but ending at different ultimate values) when element near crack tip fully fails as shown in Fig. 9(a). Thus, out of all mesh refinements, only one mesh is feasible for a fixed size of a defect in the sense that it correctly capture the fields present in the corresponding experimental specimen. The constitutive behaviour of PWTC material obtained by UMAT is thus independent of a mesh and *macro-scale* softening behaviour (after ultimate failure) is not captured (as explained earlier), no mesh regularization techniques are thus warranted in the present work. The KP values in the boundary element are thus used as an indication that correct experimental fields (stress and strain distributions) are numerically captured.

The 2D notched bar is discretized by 578 elements (CPS3) and loaded along *Y* axis to get KP values as given in Table 12.
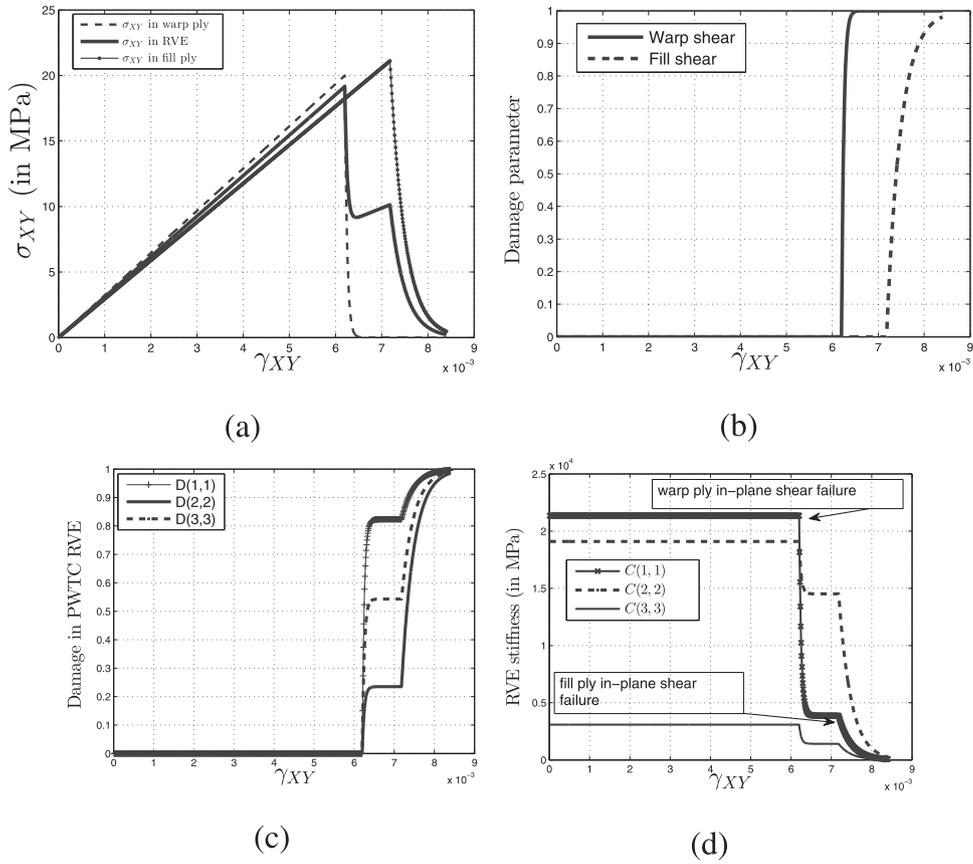
Fig. 7. PFA of PWTC by shear loading in plane $X - Y$, (a) all σ_{xy} vs γ_{xy} plots, (b) *meso-scale* damage, (c) *macro-scale* damage and (d) stiffness matrix components.
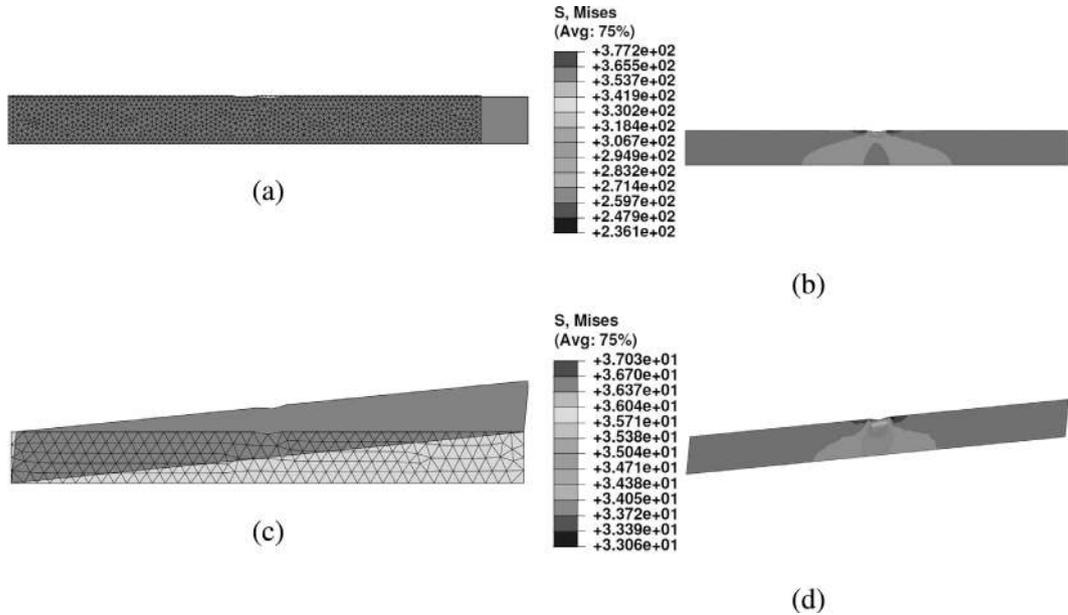
Fig. 8. Notched bar with X axis displacement solved by UMAT (a) deformation, (b) von Mises stress, shearing in $X - Y$ plane (c) deformation, (d) von Mises stress.

The 2D notched bar is discretized by 374 elements (CPS3) and loaded with γ_{XY} within global $X - Y$ plane. The nodal displacement u for the bottom and top edges are set as 0 and 0.1, respectively, and the nodal displacement v for the left and right edges are set as 0 and 0.1, respectively. The deformation and von Mises stress distribution is shown in Fig. 8(c) and (d) with KP values as given in Table 13. Another set of *in-house* axial loading experiments, by

E-glass/epoxy PWTC specimens $((v_f)_g = 0.45, (v_f^w)_g = 0.26, (v_f^F)_g = 0.19)$, are performed to demonstrate the validity of the proposed failure analysis. The numerical failure analysis is performed employing ECPL + CLT, as explained earlier, at a given GP as well as by ABAQUS® UMAT using 2D notched bar PWTC model (924 elements of type CPS3). The KP values, within GP ahead of crack tip and far-field, are obtained and all the results are tabulated in Table 14. It
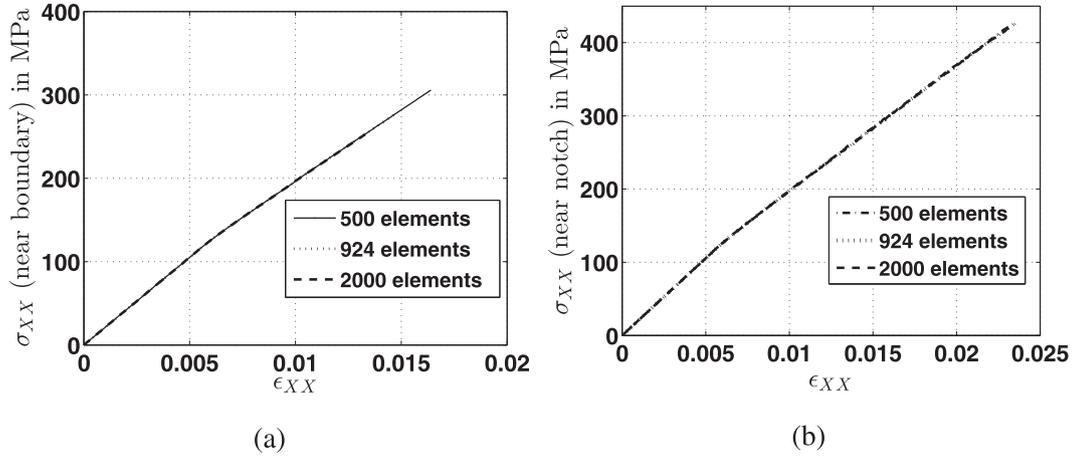
Fig. 9. *Macro-scale* results with mesh variation (a) in an element along loading boundary, (b) in an element ahead of crack tip.

Table 12
PFA of PWTC lamina by loading along Y axis (fill) (* in MPa).

Parameter KP (% ϵ_{YY}, σ_{YY}^*)	Experiment (in-house)	ECPL + CLT (Gauss point)	ECPL + CLT (UMAT)
RVE 1st KP	(0.4, 88)	(0.48, 90.23)	(0.477, 89.8)
Warp 1st KP	–	(0.48, 40.8)	(0.477, 40.6)
Fill 1st KP	–	(0.48, 143.8)	(0.477, 143.4)
RVE 2nd KP	(1.69, 263.5)	(2.35, 334.1)	(1.64, 258.8)
Fill 2nd KP	–	(2.35, 696.1)	(1.64, 487.2)

Table 13
PFA of PWTC lamina with shear loading along $X - Y$ plane (* in MPa).

Parameter KP (% γ_{XY}, σ_{XY}^*)	ECPL + CLT (Gauss point)	ECPL + CLT (UMAT)
RVE 1st KP	(0.62, 19.2)	(0.619, 19.12)
Warp 1st KP	(0.62 20)	(0.62, 19.97)
Fill 1st KP	(0.62, 18.23)	(0.62, 18.2)
RVE 2nd KP	(0.72, 10.1)	–
Fill 2nd KP	(0.72, 21.0)	–

Table 14
PFA of PWTC lamina by loading along global X axis $\left(\text{E-glass/Epoxy}, (\nu_f)_g = 0.45, (\nu_f^w)_g = 0.26, (\nu_f^F)_g = 0.19 \right)$ (*in MPa).

Parameter KP (% ϵ_{XX}, σ_{XX}^*)	Experiment (in-house)	ECPL + CLT (Gauss point)	ECPL + CLT (UMAT)
RVE 1st KP	(0.5, 113.5)	(0.5, 119.9)	(0.5, 119.3)
Warp 1st KP	–	(0.5, 184.6)	(0.5, 187.4)
Fill 1st KP	–	(0.5, 41.1)	(0.5, 40.9)
RVE 2nd KP	(1.7, 317.8)	(2.4, 469.9)	(1.5, 322.4)
Warp 2nd KP	–	(2.4, 877.8)	(1.5, 558.4)

is again observed from Table 14 that KP values in far-field element (4th column) are very close to the experimental mean values (2nd column), and KP values in element ahead of crack tip are closely matching with 3rd column (mesh independent unique constitutive behaviour).

The results obtained by UMAT closely match with experimental values, as given in Tables 11–14. The PFA of PWTC material is performed in-details in this section, and conclusions are finally drawn in the next section.

6. Conclusions

The primary focus of the present work was to study the constitutive behaviour of PWTC material (undamaged and damaged). Two homogenization models are proposed to obtain the *macro-*

scale material constants of PWTC lamina: ECPL + CLT by quarter portion of PWTC RVE, and PWTC + MT WU. The results obtained by these approaches are compared with other experiments as well as simulations.

The PFA of PWTC lamina is performed, under different loadings, coupling ECPL + CLT with IDM, and the corresponding *macro-scale* KP values are compared with experiments. The PFA by ECPL + CLT is also implemented as UMAT subroutine, and 2D PWTC notched bar model is solved in ABAQUS® under different loadings. The KP values in loading edge element are closely matching with the experimental values, whereas KP stress values near crack tip are always same as KP values correspond to PWTC lamina (*meso-scale* GP computation).

It is concluded that the proposed approaches correctly compute *macro-scale* material constants of PWTC lamina (undamaged and damaged). The present PWTC lamina model will be extended to study elasto-plastic damage in future.

Appendix A. Representation of matrices in Voigt–Mandel notation

Strain and stress tensors are represented as vectors in VM form as $\{\epsilon_{VM}\} = \left\{ \epsilon_{11}, \epsilon_{22}, \epsilon_{33}, \sqrt{2}\,\epsilon_{23}, \sqrt{2}\,\epsilon_{13}, \sqrt{2}\,\epsilon_{12} \right\}^T$ and $\{\sigma_{VM}\} = \left\{ \sigma_{11}, \sigma_{22}, \sigma_{33}, \sqrt{2}\,\sigma_{23}, \sqrt{2}\,\sigma_{13}, \sqrt{2}\,\sigma_{12} \right\}^T$, respectively, to get 2nd-order stiffness matrix. The compliance (and stiffness) matrices of all the plies are developed in local co-ordinate system in VM notation as $\{\epsilon_{VM}'\} = S_{VM}\{\sigma_{VM}'\}$. The tensorial strains $\{\epsilon_T\}$ (and tensorial stresses) are related to VM strains $\{\epsilon_{VM}\}$ (and VM stresses) as $\{\epsilon_{VM}\} = \mathcal{M}\{\epsilon_T\}$, where $\mathcal{M}$ is defined as a diagonal matrix (Udhayaraman and Mulay, 2017). The tensorial strains and stresses in local co-ordinate system are related as $\{\epsilon_T'\} = \mathcal{S}\{\sigma_T'\}$, where $\mathcal{S}$ is a 4th−order compliance tensor. The tensor $\mathcal{S}$ is obtained by matrix S_{eng} relating engineering components as $\{\epsilon_{eng}'\} = S_{eng}\{\sigma_{eng}'\} \Rightarrow \mathcal{S} = R^{-1} S_{eng}$, where R is diagonal matrix (Daniel and Ishai, 2006). The VM compliance matrix is obtained as

$$\left\{ \epsilon_T' \right\} = \mathcal{S} \left\{ \sigma_T' \right\} \Rightarrow S_{VM} = \mathcal{M} \mathcal{S} \mathcal{M}^{-1} \Rightarrow S_{VM} = \mathcal{M} R^{-1} S_{eng} \mathcal{M}^{-1} \left. \right\}$$

$$(17)$$

where S_{VM} is a VM compliance matrix in principal material-axis system of a ply.

The VM compliance matrix in global co-ordinates is obtained by transformation from local co-ordinates. Let Q be a transformation matrix, obtained by $\theta°$ CCW rotation about $Z-$axis to go to local co-ordinates (Daniel and Ishai, 2006; Udhayaraman and Mulay, 2017). The tensorial stresses in local co-ordinates are given as $(\sigma_T')_{ij} = \underbrace{Q_{im} Q_{jn}}_{M} (\sigma_T)_{mn}$, where matrix $[M]_{9 \times 9}$ is initially computed without stress tensor symmetry. M *do not* possess minor symmetry, which is also evident from the definition of M. A symmetric matrix $(Q_s)_{ijmn} = (Q_{im} Q_{jn} + Q_{in} Q_{jm})/2$ is proposed possessing minor symmetry, the stress tensor symmetry is imposed to get $[Q_s]_{6 \times 6}$. If tensorial stresses (and strains) are converted to VM stresses (and strains), then $(Q_s)_{VM}$ is obtained as

$$\sigma'_{VM} = \underbrace{\mathcal{M} Q_s \mathcal{M}^{-1}}_{(Q_s)_{VM}} \sigma_{VM} \Rightarrow (Q_s)_{VM} = \mathcal{M} Q_s \mathcal{M}^{-1} \Rightarrow$$

$$(Q_s)_{VM} = \begin{bmatrix} c^2 & s^2 & 0 & 0 & 0 & \sqrt{2}\,s\,c \\ s^2 & c^2 & 0 & 0 & 0 & -\sqrt{2}\,s\,c \\ 0 & 0 & 1 & 0 & 0 & 0 \\ 0 & 0 & 0 & c & -s & 0 \\ 0 & 0 & 0 & s & c & 0 \\ -\sqrt{2}\,c\,s & \sqrt{2}\,c\,s & 0 & 0 & 0 & (c^2 - s^2) \end{bmatrix} \tag{18}$$

such that $(Q_s)_{VM}$ is 2nd-order tensor. The matrix $(Q_s)_{VM}$ is orthogonal and $[Q_s(-\theta)]_{VM} = [Q_s(\theta)]_{VM}^T$. The VM compliance matrix in global co-ordinate system is given as $\{\epsilon_{VM}\} = \bar{S}_{VM} \{\sigma_{VM}\}$, where

$$\bar{S}_{VM} = (Q_s)_{VM}^T S_{VM} (Q_s)_{VM} \Rightarrow \bar{S}_{VM} = (Q_s)_{VM}^T \mathcal{M} R^{-1} S_{eng} \mathcal{M}^{-1} (Q_s)_{VM} \tag{19}$$

where Eq. (19) is computed by Eqs. (17) and (18).

A CCW rotation transformation matrix about global Y-axis is similarly given

$$(Q_s)_{VM} = \begin{bmatrix} c^2 & 0 & s^2 & 0 & -\sqrt{2}\,c\,s & 0 \\ 0 & 1 & 0 & 0 & 0 & 0 \\ s^2 & 0 & c^2 & 0 & \sqrt{2}\,c\,s & 0 \\ 0 & 0 & 0 & c & 0 & s \\ \sqrt{2}\,c\,s & 0 & -\sqrt{2}\,c\,s & 0 & (c^2 - s^2) & 0 \\ 0 & 0 & 0 & -s & 0 & c \end{bmatrix} \tag{20}$$

References

Aliabadi, M., 2015. Woven Composites. Computational and Experimental Methods in Structures. Imperial College Press.

Benveniste, Y., 1987. A new approach to the application of Mori-Tanaka's theory in composite materials. Mech. Mater. 6 (2), 147–157.

Bohm, H., 2016. A Short Introduction to Basic Aspects of Continuum Micromechanics. ILSB Report.

Chow, C., Wang, J., 1987. An anisotropic theory of continuum damage mechanics for ductile fracture. Eng. Fract. Mech. 27 (5), 547–558.

Daniel, I., Ishai, O., 2006. Engineering Mechanics of Composite Materials, 13. Oxford University Press.

Dixit, A., Mali, H.S., 2013. Modeling techniques for predicting the mechanical properties of woven-fabric textile composites: A review. Mech. Compos. Mater. 49 (2013), 1–20.

Eshelby, J.D., 1957. The determination of the elastic field of an ellipsoidal inclusion, and related problems. Proc. R. Soc. London A 241 (1226), 376–396.

Gitman, I., Askes, H., Sluys, L., 2007. Representative volume: Existence and size determination. Eng. Fract. Mech. 74 (16), 2518–2534.

GmbH, H. A. M. S., 2007. Araldite LY 556 / aradur 917 / accelerator DY 070 hot curing epoxy matrix system., http://www.farix.hu/pdf/1360669728.pdf.

Gommers, B., Verpoest, I., Van Houtte, P., 1998. The Mori-Tanaka method applied to textile composite materials. Acta Mater. 46 (6), 2223–2235.

Gorbatikh, L., Ivanov, D., Lomov, S., Verpoest, I., 2007. On modelling of damage evolution in textile composites on meso-level via property degradation approach. Compos. Part A 38 (12), 2433–2442.

Hill, R., 1963. Elastic properties of reinforced solids: Some theoretical principles. J. Mech. Phys. Solids 11 (5), 357–372.

Hill, R., 1965. A self-consistent mechanics of composite materials. J. Mech. Phys. Solids 13 (4), 213–222.

Huysmans, G., Verpoest, Van Houtte, P., 2004. Eshelby models applied to woven fabric composites: A benchmark study. http://www.mtm.kuleuven.ac.be/Research/C2/poly/index.htm.

Ishikawa, T., 1981. Antisymmetric elastic properties of composite plates of satin weave cloth. Fibre Sci. Technol. 15, 127–145.

Ishikawa, T., Chou, T.-W., 1982. Stiffness and strength behaviour of woven fabric composites. J. Mater. Sci. 17 (11), 3211–3220.

Jirasek, M., Marfia, S., 2005. Non-local damage model based on displacement averaging. Int. J. Numer. Methods Eng. 63 (1), 77–102.

Lemaitre, J., 1985. A continuous damage mechanics model for ductile fracture. J. Eng. Mater. Technol. 107 (1), 83–89.

Li, X., Zhang, X., Zhang, J., 2010. A generalized Hill's lemma and micromechanically based macroscopic constitutive model for heterogeneous granular materials. Comput. Methods Appl. Mech. Eng. 199 (49–52), 3137–3152.

Mori, T., Tanaka, K., 1973. Average stress in matrix and average elastic energy of materials with misfitting inclusions. Acta Metall. 21 (5), 571–574.

Naik, N., Ganesh, V., 1992. Prediction of on-axes elastic properties of plain weave fabric composites. Compos. Sci. Technol. 45 (2), 135–152.

Naik, N., Ganesh, V., 1993. Prediction of thermal expansion coefficients of plain weave fabric composites. Compos. Struct. 26, 139–154.

Naik, N., Ganesh, V., 1995. An analytical method for plain weave fabric composites. Composites 26 (4), 281–289.

Shahabi, E., Forouzan, M., 2017. A damage mechanics based failure criterion for fiber reinforced polymers. Compos. Sci. Technol. 140, 23–29.

Skoček, J., Zeman, J., Sějnoha, M., 2008. Effective properties of textile composites: application of the Mori-Tanaka method. Modell. Simul. Mater. Sci. Eng. 16 (8), 085002.

Society, A. C. Finding volume: The water displacement method, http://www.middleschoolchemistry.com/lessonplans/chapter3.

Tabatabaei, S., Bedogni, E., Ivanov, D., Lomov, S., 2014. Meso-scale damage modelling of textile composite using the embedded element technique and contact algorithm. In: 16th European Conference on Composite Materials.

Tanov, R., Tabiei, A., 2001. Computationally efficient micromechanical models for woven fabric composite elastic moduli. J. Appl. Mech. 68, 553–560.

Udhayaraman, R., Mulay, S.S., 2017. Multi-scale approach based constitutive modelling of plain woven textile composites. Mech. Mater. 112 (Supplement C), 172–192.

Voigt, W., 1889. Über die beziehung zwischen den beiden elastizitätskonstanten isotroper körper. Wied. Ann. 38, 573–587.

Wen, P., Aliabadi, M., 2009. Mesh-free micromechanical model for woven fabric composite elastic moduli. J. Multiscale Modell. 1 (2), 303–319.

Wen, P., Aliabadi, M., 2010. Elastic moduli of woven fabric composite by meshless local Petrov-Galerkin (MLPG) method. CMES: Comput. Model. Eng. Sci. 61 (2), 133–154.

Wen, P., Aliabadi, M., 2011. Damage mechanics analysis of plain woven fabric composite micromechanical model for mesh-free simulations. J. Compos. Mater. 1–15.

Xu, J., Lomov, S., Verpoest, I., Daggumati, S., Van Paepegem, W., Degrieck, J., 2015. A progressive damage model of textile composites on meso-scale using finite element method: Fatigue damage analysis. Comput. Struct. 152, 96–112.